



# Coseismic and postseismic displacements from the 1978 $M_w$ 7.3 Tabas-e-Golshan earthquake in eastern Iran

Yu Zhou<sup>a,\*</sup>, Richard T. Walker<sup>a</sup>, James Hollingsworth<sup>b,c</sup>, Morteza Talebian<sup>d</sup>, Xiaogang Song<sup>e</sup>, Barry Parsons<sup>a</sup>

<sup>a</sup> COMET, Department of Earth Sciences, University of Oxford, Oxford OX1 3AN, UK

<sup>b</sup> Université Grenoble Alpes, ISTerre, 38058 Grenoble, France

<sup>c</sup> CNRS, ISTerre, UMR 5275, 38058 Grenoble, France

<sup>d</sup> Research Institute for Earth Sciences, Geological Survey of Iran, Azadi Square, Meraj Blvd, Tehran, Iran

<sup>e</sup> State Key Laboratory of Earthquake Dynamics, Institute of Geology, China Earthquake Administration, Beijing 100029, China

## ARTICLE INFO

### Article history:

Received 16 April 2016

Received in revised form 19 July 2016

Accepted 20 July 2016

Available online xxxx

Editor: P. Shearer

### Keywords:

1978 Tabas earthquake

historical optical imagery

afterslip

characteristic slip behaviour

continental tectonics

seismic hazard

## ABSTRACT

We use optical image correlation of historical aerial photographs, and modern satellite images to investigate the 1978  $M_w$  7.3 Tabas-e-Golshan thrust earthquake in eastern Iran. Correlation of images between 1974 and 1991 reveals a near-surface shortening component of  $\sim 2.9$  m across the margin of the Tabas fold, which is a combination of coseismic and postseismic deformation. Correlation of images between 1991 and 2013 shows a further  $\sim 0.3$  m of postseismic shortening. Using six pre-earthquake aerial photographs acquired in 1956 and stereo SPOT-6 imagery from 2013, we also generate pre- and post-earthquake digital elevation models (DEMs) for one of the main fold segments. Differencing of the two DEMs reveals a height change of  $\sim 4.7$  m. Elastic dislocation modelling of the 1974–2013 displacement field requires 7 m slip on a  $50^\circ$  dipping fault, extending from a depth of 0.1 km to 6 km at its base (the majority of slip,  $\sim 6.5$  m, occurred prior to 1991). Our results, combined with previous InSAR observations, indicate time-decaying shallow postseismic afterslip. It is likely that most of the afterslip occurred prior to 1991. The slip appears to dissipate in the near surface, and is accommodated as a narrow band of flexural slip on bedding planes. Comparison of the fault slip model with terrace heights measured from the SPOT-6 DEM suggests that the Tabas fold system may exhibit characteristic slip behaviour. Such behaviour would require a magnitude  $M_w$  7.3 earthquake every  $\sim 3500$  years, based on the previously estimated shortening rate of  $\sim 1.0$  mm/yr. This study highlights the usefulness of historical imagery in investigating past earthquakes, thus providing new information about historical faulting in continental regions.

© 2016 Elsevier B.V. All rights reserved.

## 1. Introduction

Measurements of surface deformation in earthquakes and by postseismic creep reveal how active folds and faults evolve over the seismic cycle (Burbank and Anderson, 2011; Copley, 2014; Dolan et al., 2003; Yu et al., 2003). They provide the most valuable source of data for the accurate description and understanding of continental tectonics, and for investigating present and future seismic hazard (Berberian, 1981; Hubbard and Shaw, 2009; Molnar and Lyon-Caen, 1989; Molnar et al., 1973; Tapponnier et al., 1990). Large continental earthquakes ( $M_w \geq 7$ ) often occur on faults that were previously unmapped or poorly studied, due to the long re-

currence times between events and their subtle geomorphological expression in the landscape (England and Jackson, 2011; Fialko et al., 2005; Funning et al., 2005; Jackson, 2001; Oskin et al., 2012; Zhang, 2013; Zhou et al., 2015a). Large blind thrust earthquakes, e.g. the 2015 Gorkha earthquake in Nepal (Elliott et al., 2016; Feng et al., 2015; Grandin et al., 2015; Wang and Fialko, 2015), have been uncommon in the era of modern satellite geodesy. Due to their hazardous nature, there is a strong need to re-examine older events to improve our understanding of the factors controlling the rupture of blind thrust faults.

The September 16, 1978  $M_w$  7.3 Tabas-e-Golshan earthquake in eastern Iran (hereafter referred to as the Tabas earthquake) is an example that occurred prior to the onset of interferometric synthetic aperture radar (InSAR) and Global Positioning System (GPS) monitoring, rupturing a series of previously unrecognised blind thrust faults. It is the only known large event in

\* Corresponding author.

E-mail address: [yu.zhou@earth.ox.ac.uk](mailto:yu.zhou@earth.ox.ac.uk) (Y. Zhou).

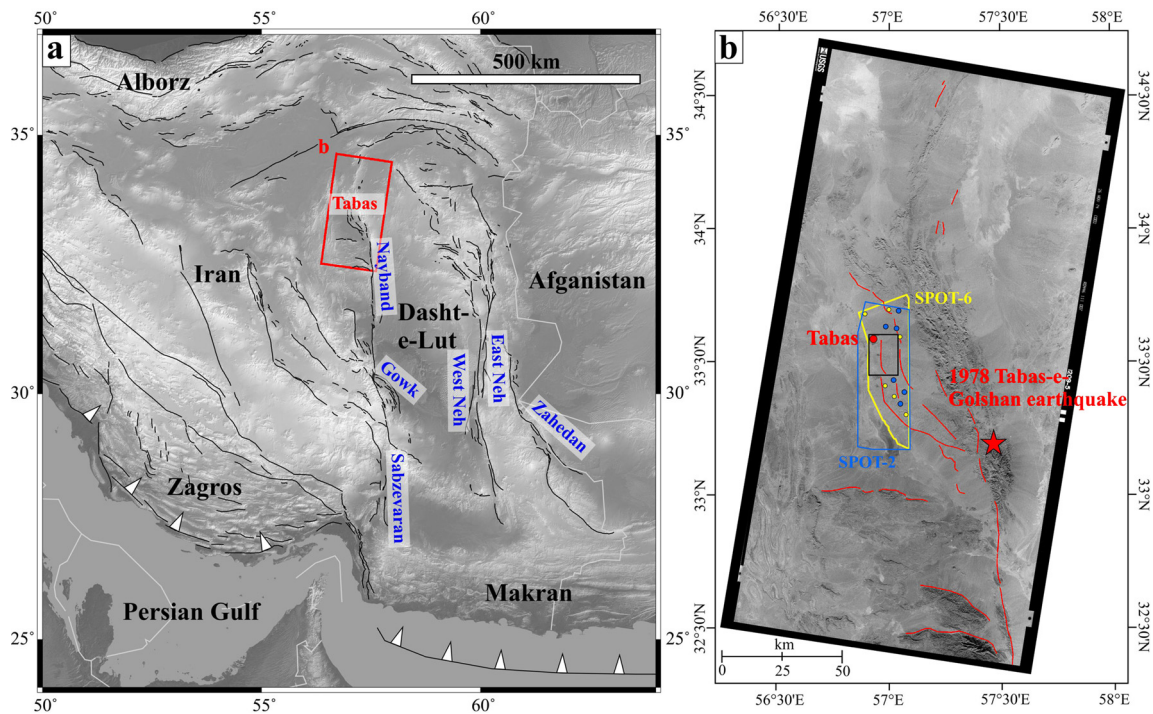


**Fig. 1.** (a) Active faults (black lines) in Iran, from Walker et al. (2003). Red box shows the coverage of the pre-earthquake KH-9 image. (b) KH-9 image around the Tabas region. Red star indicates the epicentre of the 16 September, 1978 Tabas-e-Golshan earthquake, from Walker et al. (2003). Red lines are active faults. Red dot indicates the location of Tabas. Yellow polygon shows SPOT-6 stereo image coverage (Fig. 2b). Yellow circles show the location of the GCPs used to co-register the KH-9 and SPOT-6 images. Blue polygon shows the SPOT-2 image coverage that we purchased for this study, with blue circles indicating the GCPs used to co-register the SPOT-2 and SPOT-6 images. Black box shows the area of Fig. 3a. (For interpretation of the references to colour in this figure legend, the reader is referred to the web version of this article.)

the epicentral area for at least the last 1,000 years, and completely demolished the oasis town of Tabas, killing ~11,000 people, 85% of its population (Berberian, 1979; Berberian et al., 1979; Walker et al., 2003, 2013).

Berberian (1979) mapped 85 km of discontinuous surface ruptures 10 days after the 1978 earthquake. Much of the surface faulting took the form of small amounts of slip on multiple bedding planes, suggesting that much of the slip at depth failed to reach the surface and was instead accommodated as flexural-slip folding. The maximum coseismic vertical displacement localised on the main frontal thrust fault on the segment south of Tabas was measured to be ~35 cm, but adjacent bedding slip totalled ~150 cm (Berberian, 1979). Because most of the coseismic slip was concentrated at depth (Berberian, 1982; Walker et al., 2003), it is not possible to determine the pattern and magnitude of seismogenic slip and the sub-surface structure from mapping of discrete surface ruptures alone. No geodetic measurements of coseismic displacement exist, since GPS and InSAR monitoring were not available at the time of the 1978 Tabas earthquake. Nevertheless, Copley (2014) used InSAR to image shallow creep on the fold ~6 km S-E of the town of Tabas (hereafter referred to as the Tabas fold) 30 years after the event.

The declassification of US Hexagon Keyhole-9 imagery (hereafter referred to as KH-9) allows us to investigate historical earthquakes back to the early 1970s (Burnett, 2012; Hollingsworth et al., 2012) as they provide a visual record of the landscape prior to the earthquake. In this study, we use sub-pixel optical image correlation to retrieve the coseismic and postseismic deformation fields. We first correlate KH-9 images acquired in 1974 with SPOT-2 satellite images acquired in 1991, and also modern high-resolution SPOT-6 data, to determine the horizontal displacements associated with the 1978 Tabas earthquake, from which we invert for the fault structure and earthquake slip. We also use six pre-earthquake aerial photographs acquired in 1956 and a post-earthquake SPOT-6 stereo data set acquired in 2013 to generate

the pre- and post-earthquake topography respectively for one of the main fold segments (the same one as Copley, 2014). By differencing the pre- and post-earthquake topography, we measure the coseismic and postseismic height changes which allow us to better constrain the fault slip model. By reconciling our best-fit fault slip model with analysis of the long-term surface folding observed in the SPOT-6 topography, we constrain the 3D evolution of active thrust faulting in this region throughout the Late Quaternary.

## 2. Tectonic background of the 1978 Tabas earthquake

Iran is actively deforming in response to the collision of Arabia with Eurasia at a rate of ~25 mm/yr at longitude 60° (Vernant et al., 2004a; Walker and Jackson, 2004). Regional deformation is characterised by distributed folding, reverse faulting, and strike-slip faulting (Berberian, 1981; Jackson et al., 1995; Walker and Jackson, 2004) (Fig. 1a). Studies based on plate models and GPS measurements indicate that up to half of the total Arabia-Eurasia shortening is taken up by north-south shortening in the Zagros mountains of southwestern Iran (~10–15 mm/yr) (Hessami, 2002; Jackson et al., 1995; Tatar et al., 2002; Walpersdorf et al., 2006) with the Alborz accommodating a further  $5 \pm 2$  mm/yr north-south shortening (Vernant et al., 2004b) and subduction of the South Caspian for another ~5–10 mm/yr (Hollingsworth et al., 2008). The northward motion of central Iran relative to western Afghanistan results in ~15 mm/yr north-south right-lateral shear (Mousavi et al., 2013; Walker and Jackson, 2004; Walpersdorf et al., 2014), accommodated across several right-lateral strike-slip faults bordering the Dasht-e-Lut Desert in eastern Iran. These include the East Neh (1.75–2.5 mm/yr from Meyer and Le Dortz, 2007), West Neh (1–5 mm/yr from Meyer and Le Dortz, 2007) and Zahedan faults in the east, and the Sabzevaran (~6 mm/yr from Regard et al., 2006), Gowk (~3.8–5.7 mm/yr from Fattahi et al., 2014; Walker et al., 2013) and Nayband (~1.4 mm/yr from Walker et al., 2009 and ~1.8 mm/yr from Foroutan et al., 2014) segments

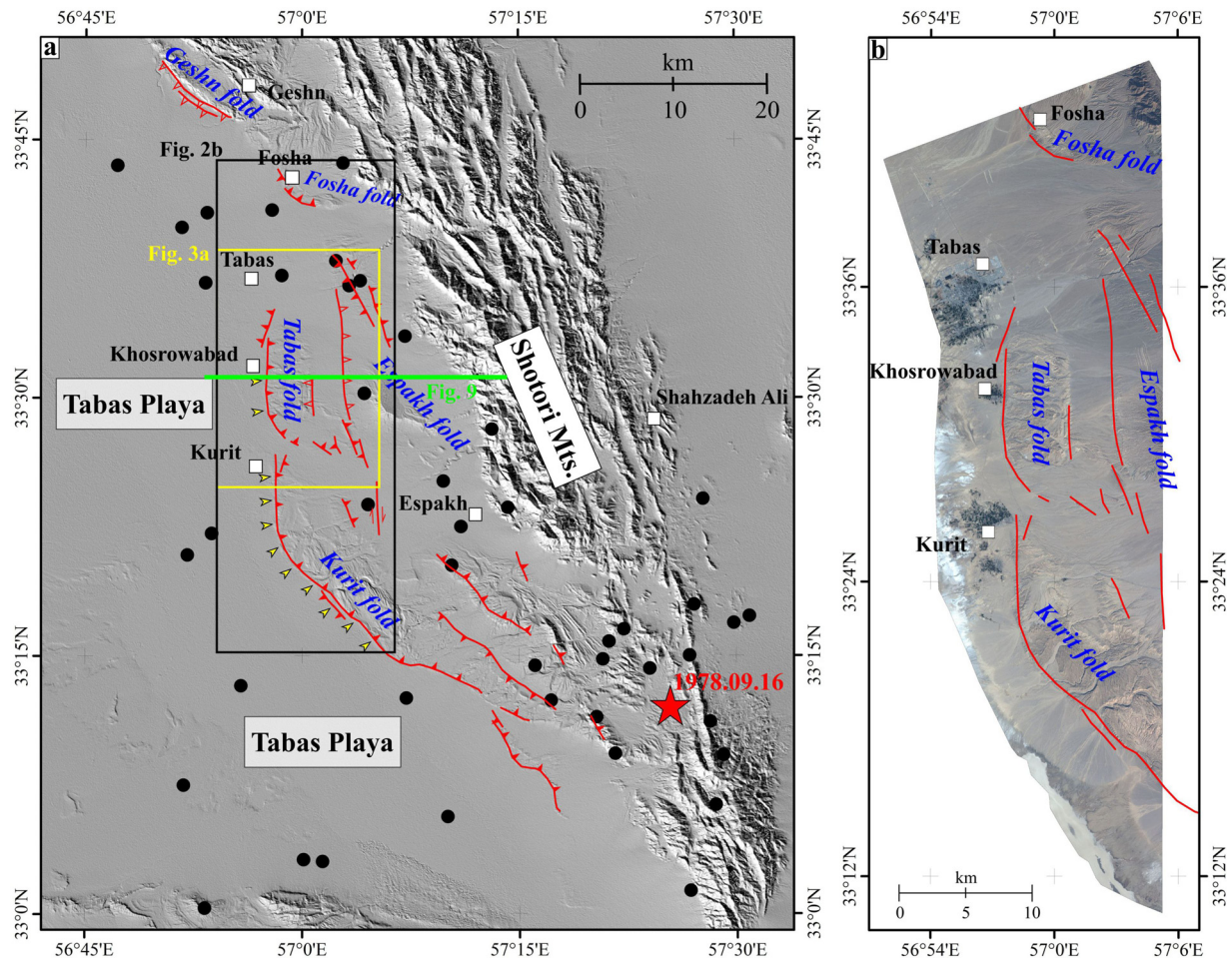


**Fig. 2.** (a) Surface ruptures (red lines) observed in the field by Berberian (1979). Red filled triangles denote thrust faulting and open triangles are high-angle reverse faulting. Yellow arrows mark the segments that show afterslip in Copley (2014). Black dots are the epicentres of smaller earthquakes, from Walker et al. (2013). Green line shows the location of the topographic profile in Fig. 8. (b) SPOT-6 orthoimagery showing the epicentral area of the 1978 Tabas earthquake. See (a) for location. (For interpretation of the references to colour in this figure legend, the reader is referred to the web version of this article.)

in the west (Fig. 1a). The 1978 Tabas earthquake occurred at the northern end of the Nayband fault where north–south right-lateral strike-slip motion turns into a zone of distributed thrusting that is manifest at the surface as a series of folds within Neogene basin deposits.

The Tabas region had been quiescent for at least 1,100 years until the 1978 earthquake (Berberian, 1979). Detailed field mapping 10 days after the earthquake (Berberian, 1979) revealed extensive slip on folded Neogene bedding planes along the 85 km-long system of folds, and some high-angle faults within the folds that are likely tensional features (Fig. 2), consistent with coseismic fold growth (e.g. Walker et al., 2003). Berberian (1979) also measured a maximum displacement of  $\sim 35$  cm along a discrete east-dipping reverse fault at the western margin of the Kurit fold segment (Fig. 2). Assuming a single, simple rupture event, Walker et al. (2003) estimated an average slip of  $\sim 3.3$  m using a rupture velocity of  $\sim 3.5$  km/s, main shock source time function duration of 18 s, and typical ratio of average slip to rupture length ( $\bar{\mu}/L$ ) of  $5 \times 10^{-5}$  (Scholz, 1982). The relatively small surface slip measured in the field ( $\sim 35$  cm) implies that most of the coseismic slip at depth failed to reach the surface (Walker et al., 2003). The source parameters of the main shock indicate slip on a detachment thrust fault dipping  $\sim 16^\circ$ E with a centroid depth of  $\sim 9$  km and with an epicentre southeast of the folding (Walker et al., 2003, 2013). Analysis of 329 aftershocks shows a concentration of events around depths of 5–10 km (Berberian et al., 1979). Copley (2014) esti-

mated  $\sim 5$  mm/yr postseismic afterslip on a steep ramp beneath the Tabas fold, extending to a depth of 4–5 km, from modelling InSAR observations in the interval 1996–1999 (Fig. 2). By combining all the available information, and assuming that postseismic afterslip decays with time rapidly (Segall et al., 2000), Copley (2014) inferred that the majority of the slip gradient was relaxed aseismically prior to 1996 by postseismic motion on a high-angle thrust ramp that connects the surface anticlines to the coseismic low-angle detachment fault at depth.

### 3. Image processing

To measure the surface displacement associated with the 1978 Tabas earthquake, we first obtained a KH-9 image acquired in 1974, six aerial photographs taken in 1956, a SPOT-2 image from 1991 and a SPOT-6 stereo data set from 2013 (listed in Table 1). Correlation of the KH-9 and SPOT-2 imagery provides information about the coseismic and relatively early postseismic horizontal motion, whereas the SPOT-2 and SPOT-6 imagery can be used to measure the horizontal motion in the later postseismic period. All correlations include some component of postseismic motion as the earliest post-earthquake imagery we use was acquired 13 years after the main shock.

Furthermore, we use the aerial photographs to generate a pre-earthquake digital elevation model (DEM) from 1956 and the stereo SPOT-6 imagery to generate a post-earthquake DEM from 2013. By differencing the two DEMs, we can also measure the

**Table 1**  
Images used in this study.

	Pre-earthquake		Post-earthquake	
	KH-9	Aerial	SPOT-2	SPOT-6
Time	9th Mar., 1974	13th Aug., 1956	6th Sep., 1991	29th Dec., 2013
Type	Frame camera	Frame camera	Pushbroom	Pushbroom
Resolution (m)	6–9	1–3	10	1.5
Focal length (cm)	30.5	15.524		

height changes between 1956 and 2013. In this section, we describe the methods of processing these various images.

### 3.1. SPOT-6 images obtained in 2013

The SPOT-6 satellite was launched on the 9th September 2012, in a sun-synchronous orbit with a repeat cycle of 26 days (Astrium, 2013). It can provide 1.5 m resolution panchromatic and 6 m resolution multispectral images over a swath footprint of 60 km for high-resolution stereo mapping (Astrium, 2013). We purchased one tri-stereo data set tasked on the 29th December 2013 over an area of 918 km<sup>2</sup> (Fig. 1b). Provided with the rational function models of the three SPOT-6 images, we processed the data using the Leica Photogrammetry Suite (LPS) with a pairwise pixel-by-pixel matching procedure (see Supplementary Material for details) (Zhou et al., 2015b). The point cloud extracted from the new automatic terrain extraction module (eATE) in LPS was filtered by averaging within a cell of 2 m and then gridded with a pixel spacing of 2 m (coordinate system: WGS84 UTM 40N). The SPOT-6 image was then orthorectified using the 2 m DEM. The SPOT-6 orthoimage (Fig. 2b) is used as the reference image for co-registration of all earlier imagery in the following sections.

### 3.2. KH-9 image obtained in 1974

The KH-9 mapping program consisted of 12 missions (mission numbers: 1205–1216) (Burnett, 2012). The first mission (1205) was operational from the 9th March 1973 to the 20th April 1973, with a duration of 42 days (Burnett, 2012). Many subsequent missions followed, before the program ended on the 14th October 1980, having amassed a total of ~29000 images with a resolution of 6–9 m globally. Each KH-9 image has a footprint of 125 km × 250 km, and is available for purchase from the USGS EarthExplorer website for \$30. However, detailed information about the camera system used for earth mission, such as focal length, optical distortions and film size is unavailable. It has been concluded from different experiments that KH-9 uses a camera similar to the NASA Large Format Camera (LFC), a 23 cm × 46 cm frame camera with a focal length of 30.5 cm (Hollingsworth et al., 2012; Mollberg and Schardt, 1988; Surazakov and Aizen, 2010).

Fig. 1b shows a KH-9 image covering the Tabas region, acquired on the 26th November 1974 (mission 1209). No post-earthquake KH-9 imagery is available for the Tabas region. The KH-9 image was processed using the aerial photo module of COSI-Corr (Ayoub et al., 2009). We first used a bilinear interpolation to resample the SPOT-6 orthoimage to 6 m to match the lower resolution KH-9 image. The KH-9 image was then co-registered to the 6 m SPOT-6 orthoimage using 7 ground control points (GCPs) collected 10–20 km from the Tabas fold, where the maximum surface displacement was observed in the field (Berberian, 1979) and the postseismic interferograms (Copley, 2014). In the absence of a suitable pre-earthquake DEM, the KH-9 image was orthorectified using the post-earthquake SPOT-6 DEM (the DEM generated from the pre-earthquake aerial photographs contains large errors due to tilting and various distortions including scanning, optical and film distortions, discussed in Section 4.2). As a result, any height changes will cause an apparent horizontal signal (discussed in Hollingsworth

et al., 2012 and Barišič et al., 2015). In our case, this influence ( $\leq 0.5$  m) is insignificant compared to the tectonic signal ( $\sim 3.5$  m) because the location of the Tabas fold within the KH-9 image is close to the centre, as discussed in Supplementary Material.

### 3.3. SPOT-2 in 1991

The SPOT-2 satellite was launched on the 22nd January 1990, and deorbited in July 2009. The products, including 10 m resolution panchromatic and 20 m resolution multispectral images, were acquired over a swath footprint of 60 km. Fig. 1b shows the coverage (1000 km<sup>2</sup>) of the SPOT-2 panchromatic image that we purchased for this study. It was acquired on the 6th September 1991 with an incidence angle of  $-2.2^\circ$ . Following the same procedure as described in Section 3.2, we co-registered the SPOT-2 image to the SPOT-6 orthoimage using 6 GCPs (as shown in Fig. 1b) and orthorectified it using the SPOT-6 DEM.

### 3.4. Aerial photographs obtained in 1956

Six aerial photographs covering the Tabas region were acquired on the 13th August, 1956, as part of a country-wide survey. The aerial photographs were scanned from print copies at a resolution of 1200 dpi × 1200 dpi using an EPSON Expression 1100XL scanner. We orthorectified the aerial photographs using a frame camera model in LPS to generate a pre-earthquake DEM. Interior orientation parameters consist of the focal length and the location of the principal point. The focal length (155.24 mm) is provided with the photograph, and the location of the principal point was estimated using the fiducial points on the four edges of each image. The exterior orientation parameters (the location, elevation, and three rotation angles of the camera) were estimated with a least-squares adjustment using 36 GCPs identified from the SPOT-6 imagery and DEM, along with 108 tie points (points whose ground coordinates are unknown, but are common to both images). After having solved the orientation parameters for all aerial photographs, we extracted a DEM (5 m spatial resolution) with eATE in LPS (see Supplementary Material for the aerial DEM).

## 4. Results

### 4.1. Horizontal displacement from image correlation

We estimated horizontal displacements by correlating the KH-9 (resampled to 6 m), SPOT-2 (resampled to 6 m) and SPOT-6 (resampled to 6 m) images in COSI-Corr (Leprince et al., 2007). A multi-scale correlation window of 64 pixels was used, followed by 32 pixels, with a step of 8 pixels (48 m) (Ayoub et al., 2009). COSI-Corr can measure surface displacements with sub-pixel precision (Hollingsworth et al., 2012; Leprince et al., 2007; Zhou et al., 2015b). We also tested different parameters in the correlation procedure (see Fig. S2 in Supplementary Material), and the results from alternative correlation window sizes (32 × 32 pixels or larger) all show a similar dislocation pattern, increasing our confidence in the validity of the results.

In this study, we focused on the north–south striking Tabas fold for three reasons: (1) although the N–S displacement field was

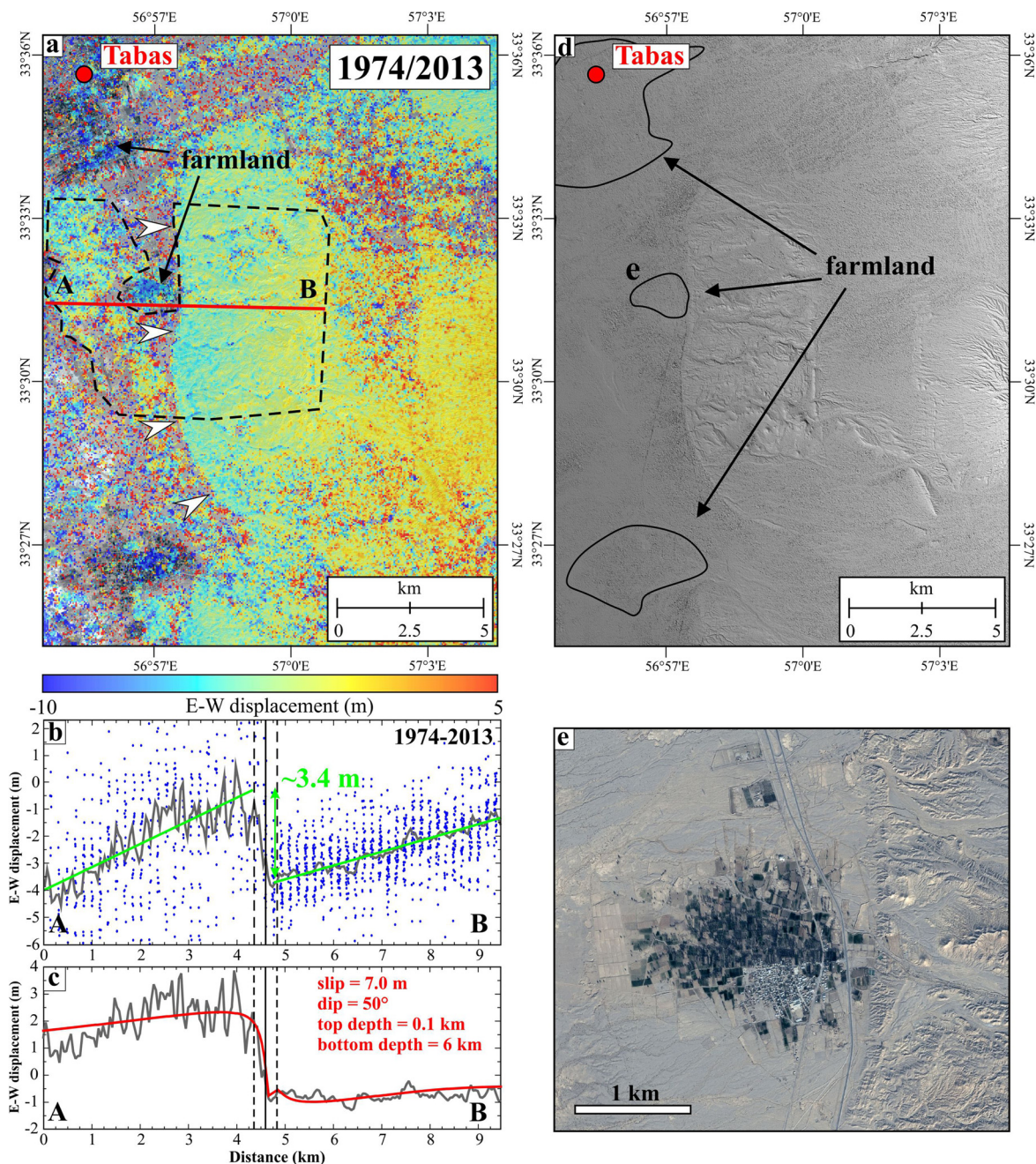


**Fig. 3.** E–W displacement from correlating the KH-9 and SPOT-6 images. See Fig. 2 for location. (a) E–W displacement map. White arrows indicate the deformation front. We projected the measurements included in the dashed polygon onto line AB and took the average in 50 m wide along-profile bins to estimate the displacement (i.e. shortening). Large deformation signals (blue areas) in the Tabas playa are due to farming. Red circle indicates Tabas. (b) Profile AB (gray line) shows a 3.4 m E–W displacement across the fold estimated by fitting two lines (green lines) on each side of the fault. Blue dots show the raw data points in (a). The measurements in the footwall are more scattered due to decorrelation of some pixels within the swath (white noise), and averaging cannot reduce these noises. (c) Displacements predicted with the Okada model of uniform slip on a rectangular fault plane. The best-fitting model through grid search (red line) is 7 m slip on a fault, dipping  $50^\circ$  beneath depths of 0.1 km to 6 km at its base. The model agrees very well with our measurement in the hanging wall, whereas the slightly larger misfit in the footwall is caused by decorrelation (white noise). (d) Shaded-relief SPOT-6 DEM showing the same region as (a). (e) SPOT-6 imagery showing farmland. (For interpretation of the references to colour in this figure legend, the reader is referred to the web version of this article.)

heavily contaminated by the scanning artifacts (see Fig. S1 in Supplementary Material), the E–W displacement field, which contains all of the tectonic signal, is free from such contamination; (2) it is located in the centre of the image, where the incidence angle is close to nadir, thereby minimising topographic residuals which can contaminate the horizontal displacement fields (see Supplementary Material); (3) we have constraints on the fold structure from inversion of postseismic InSAR.

Figs. 3a, 4a and 4d show the E–W displacement fields across the Tabas fold over different time intervals. In general, the relatively

old alluvial materials within the fold and the minimal vegetation cover result in high coherence in the correlations even 35 years after the earthquake. Despite the longer time interval, the correlation result from the high-resolution imagery (SPOT-6) (Fig. 3a) is much less noisy than that from the lower-resolution imagery (SPOT-2) (Fig. 4a). To determine the displacement, we projected all the measurements onto the fault-perpendicular direction (line AB in Fig. 3a), and averaged the data in 50 m wide bins to increase the signal-to-noise ratio. By doing so, we obtained a displacement profile for each correlation result. There are some large localised

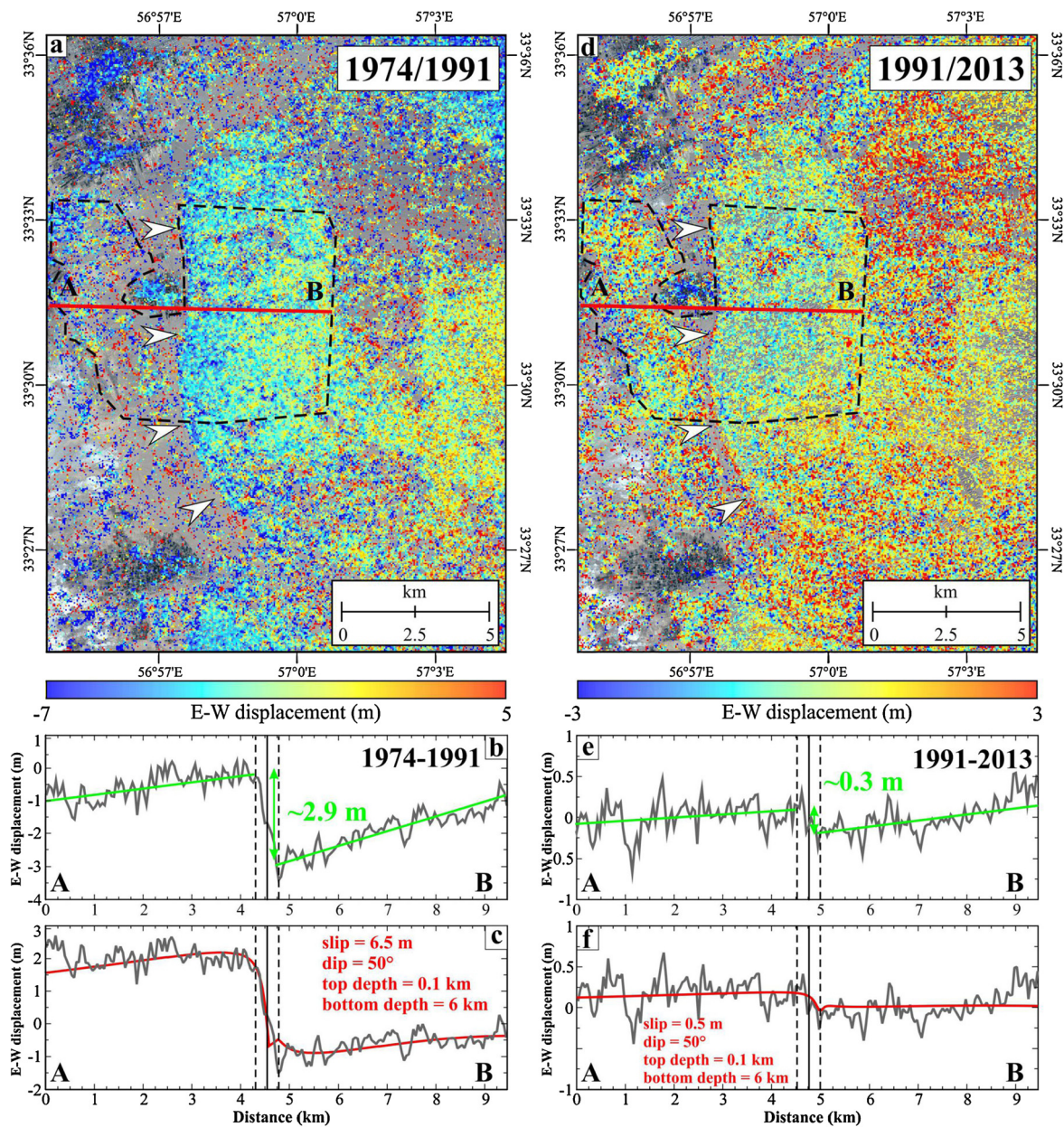


**Fig. 4.** (a)–(c) As for Fig. 3, but using the KH-9 and SPOT-2 images. Profile AB shows a  $2.9 \pm 0.2$  m E–W displacement. We fixed the fault geometry and varied the slip to reproduce this displacement. The best-fitting model gives a slip of 6.5 m. (d)–(f) As for Fig. 3, but using the SPOT-2 and SPOT-6 images. Profile AB shows a  $0.3 \pm 0.1$  m E–W displacement. We fixed the fault geometry and varied the slip to reproduce this displacement. The best-fitting model gives a slip of 0.5 m.

westward displacements (negative values) over agricultural areas, which appear to be caused by subsidence due to water pumping (see Section 3 in Supplementary Material), so we masked out those areas and only used the data points included in the dashed polygon. From the displacement profile in Fig. 3b, we found an E–W offset of  $3.4 \pm 0.3$  m (i.e. shortening) from 1974 to 2013. Most of the displacement ( $2.9 \pm 0.2$  m) occurred over the interval 1974–1991 (Fig. 4b), with a small amount ( $0.3 \pm 0.1$  m) over the interval 1991–2013 (Fig. 4e). These displacement profiles are used to determine the fault geometry and slip at depth in Section 5.1.

#### 4.2. Height changes from DEM differencing

By differencing the pre-earthquake DEM generated from the aerial photographs and the post-earthquake SPOT-6 DEM, we also measured the height changes between 1956 and 2013. The elevation differences in Fig. 5a show warping at the edge of each

aerial photograph which covers part of the mosaic. These are non-tectonic signals in the pre-earthquake DEM, caused by the strong radial distortions at the edge of the images, problems with matching pixels with large differences in incidence angles in these areas, and film distortions (e.g. bending) due to duplication and storage over almost six decades. The resulting elevation errors in the pre-earthquake DEM can be as large as several metres, so we did not use the aerial photographs and the DEM for image matching. Also, we did not account for the horizontal motion in DEM differencing because (1) we cannot solve the horizontal displacements between the two DEMs, and (2) the area is relatively flat with a regional slope of  $\leq 2^\circ$  (see the topographic profiles in Fig. 9b), which means that the horizontal displacements would not cause large apparent vertical motion.

Despite the large long-wavelength film distortions in Fig. 5a, we can still measure the shorter-wavelength dislocation at the fold front. We projected the elevation differences in the area

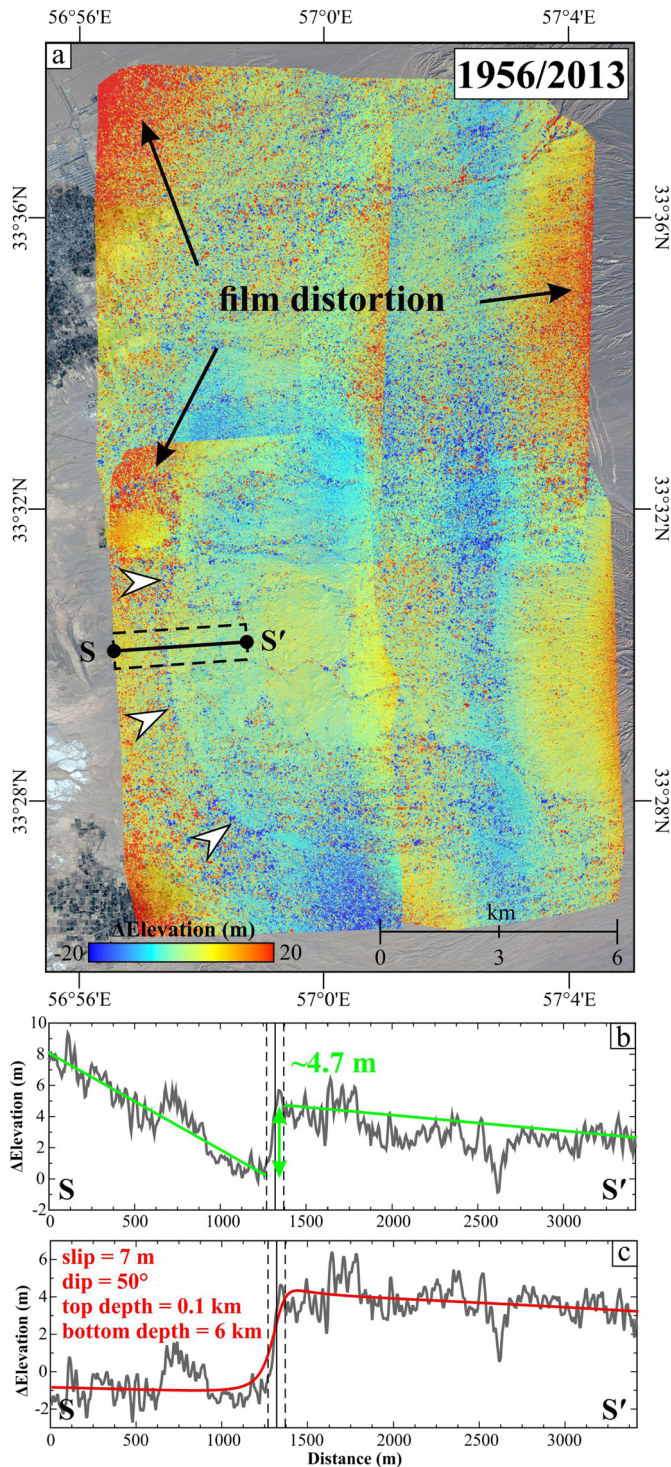


**Fig. 5.** Height changes from direct differencing of the pre-earthquake aerial DEM and the post-earthquake SPOT-6 DEM. (a) Height change map. White arrows indicate the deformation front. We projected the measurements included in the polygon onto line  $SS'$  and took the average in along-profile bins to estimate the displacement. (b) Profile  $SS'$  shows a 4.7 m height change (gray line) estimated by fitting two lines (green lines) on each side of the fault. (c) Height changes predicted with the Okada model of 7 m slip on a rectangular fault plane, dipping  $50^\circ$  beneath depths of 0.1 km to 6 km at its base. A third-order polynomial was fitted based on the residuals between the predicted displacement and the measured profile, and then removed to compensate for the film distortions. The prediction (red line) agrees well with our estimate. (For interpretation of the references to colour in this figure legend, the reader is referred to the web version of this article.)

where we measured the horizontal displacements onto the fault-perpendicular direction (line  $SS'$  in Fig. 5a). Profile  $SS'$  in Fig. 5b shows a height change of  $\sim 4.7$  m at the fault over the interval 1956–2013.

## 5. Discussion

### 5.1. Models of fault slip

Based on the earthquake surface deformations, we are able to model the fault geometry and slip at depth, using an elastic dislocation approach (Okada, 1985). For the modelling, we assume constant slip on a rectangular plane to estimate the geometry and slip of the faulting. As the KH-9 and SPOT-6 correlations have good coherence (Fig. 3), we use this result for determining the fault model. We varied the depth to the top of the fault plane from 0–0.5 km in steps of 0.1 km, the depth to the bottom from 4–10 km in steps of 1 km, the dip from  $40$ – $80^\circ$  in steps of  $5^\circ$  and fault slip from 3–9 m in steps of 0.5 m. The strike and rake were fixed to  $2^\circ$  and  $90^\circ$  (i.e. pure thrust motion). We then performed a grid search to find the best fit to our measurement. Because we do not have any reference point in the displacement field, a linear trend is evident in the measured profile (Fig. 3b). We computed the residuals between each Okada model and the measured profile, and fitted a linear trend based on the residuals. We then removed the linear trend from the measured profile, and recalculated the residuals between the predicted displacement and the new profile. As the data is noisy, we are limited in what we can resolve in the modelling. The solution with minimum misfit (the standard deviation of the residuals) gave  $7 \pm 0.5$  m slip on a  $50 \pm 5^\circ$  dipping fault, from a depth of 0.1 km to  $6 \pm 1$  km at its base (Fig. 3c). We give examples of the fits of other models in Supplementary Material. This fault geometry is consistent with that obtained by modelling the postseismic deformation observed using InSAR (Copley, 2014), i.e. a dip of  $55 \pm 10^\circ$  and bottom depth of  $\sim 4$ – $5$  km. Note that Copley (2014) modelled surface slip, i.e. a top depth of 0 km, but this model does not fit the displacement from image correlation, as shown in Fig. S4 in Supplementary Material. Our model with a top depth of 0.1 km is more consistent with the measurement, which suggests that the main fault slip did not reach the surface.

We also calculated the theoretical height change, and compared it to the measurement from DEM differencing. As explained in Section 4.2, the mismatch between the modelled height change and profile  $SS'$  is caused by a combination of a lack of reference points and film distortions in the aerial photographs. We modelled the distortion function as a third-order polynomial (Brown, 1971) and calculated the coefficients of the polynomial based on the residuals between the Okada model and the measured profile. The polynomial was removed from profile  $SS'$  (Fig. 5c). Similarly, we performed a grid search procedure and obtained 7 m slip on a  $50$ – $60^\circ$  dipping fault, from a depth of 0.1 km to  $\sim 5$ – $7$  km at its base (Fig. 5c), providing an additional constraint on the fault slip model.

As the KH-9 and SPOT-2, and SPOT-2 and SPOT-6 correlations are much noisier, we did not use them to model the fault geometry. Instead, we used the best-fitting fault geometry obtained from the KH-9 and SPOT-6 correlations (a fault plane with a strike and dip of  $2^\circ/50^\circ$ , from a depth of 0.1 km to 6 km at its base), and repeated the modelling procedure to determine the total slip in the intervals 1974–1991 and 1991–2013 by varying the magnitude of slip in steps of 0.25 m. Similarly, a linear trend was fitted based on the residuals between the prediction and the displacement profile, and removed from the displacement profile before comparing the models and the measurement, i.e. inverting for the linear ramp, as well as the slip values. Based on the minimum misfit, we found 6.5 m slip in the coseismic and early postseismic





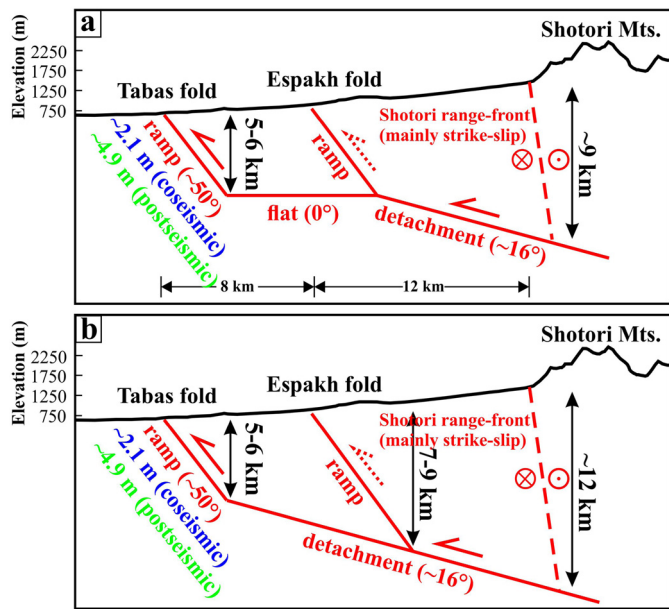


**Fig. 8.** Schematic cross-section of faults in the Tabas region. See Fig. 2 for location. As the subsurface structure of the Espakh fold is not well constrained by the uplift of the river terrace only, we show two possible scenarios of faulting in the region. (a) The Tabas and Espakh folds are connected by a flat at a depth of  $\sim 5\text{--}6$  km. The flat shallows into the detachment (dipping at  $\sim 16^\circ$  from Walker et al., 2003), which joins the Shotori range-front fault at a depth of  $\sim 9$  km ( $6\text{ km} + 12\text{ km} \times \tan 16^\circ$ ). Vertical displacements across the Tabas fold measured by Berberian (1979) indicate that the coseismic slip on the Tabas ramp accounts for  $\sim 30\%$  of the total slip. Therefore, we speculated the coseismic slip on the fault plane is  $\sim 2.1$  m, with a postseismic afterslip of  $\sim 4.9$  m. (b) As for (a), but the Tabas and Espakh folds are connected by the detachment (dipping at  $\sim 16^\circ$ ). This scenario requires the Espakh reaches a depth of  $7\text{--}9$  km, and the Shotori range-front fault joins the detachment at a depth of  $\sim 12$  km ( $6\text{ km} + 20\text{ km} \times \tan 16^\circ$ ).

ment fault with a centroid depth of 9 km with the epicentre under the Shotori Mountains (Walker et al., 2003). Vertical displacements at the western margins of the Tabas and Espakh folds are the result of slip on associated ramps, which are connected by a flat at a depth of  $\sim 5\text{--}6$  km (Fig. 8a). The flat shallows into the detachment that joins the Shotori range-front fault at a depth of  $\sim 9$  km ( $6\text{ km} + 12\text{ km} \times \tan 16^\circ$ , Fig. 8a). Given the fact that we do not have constraints on the subsurface structure of the Espakh fold, it is also possible that both ramps are connected by a planar detachment fault (dipping  $16^\circ$ ) (Fig. 8b), which would require that the Espakh fault reaches a depth of  $\sim 7\text{--}9$  km, and the Shotori range-front fault joins the detachment at a depth of  $\sim 12$  km ( $6\text{ km} + 20\text{ km} \times \tan 16^\circ$ , Fig. 8b).

#### 5.4. Long-term surface folding: characteristic slip behaviour

The SPOT-6 DEM also enables us to analyse the long-term surface folding. We identified two river terraces (a younger terrace T1 and an older one T2) associated with the growth of the Tabas fault. Fig. 9 shows three topographic profiles, S1–S1' along a modern river channel, S2–S2' along the T1 surface, and S3–S3' along the T2 surface. As the topography is dominated by a depositional slope of the alluvial surface, we removed a regional gradient from each profile, as shown in Figs. 9c–9e. Note that because only a fragment of T2 is preserved, we extended S3–S3' onto the T1 surface in order to calculate the regional surface slope. We chose river channel S1–S1' for analysis because (1) unlike the big rivers, where the relatively young alluvial fans (T1 and T2) have been washed away, fragments of T1 are seen here (Figs. 9a) which indicates that the river is likely to preserve recent earthquake motion, and (2) walls and dams have been built across other rivers to suppress floods and may have also changed the sedimentation and erosion

patterns since the earthquake. The other rivers in the area do not show visible warping for the reasons outlined above.

The uplift profiles (Figs. 9c–9e) indicate that warping of the river channel and both terraces occurs over a distance of  $\sim 6\text{--}7$  km, similar to that expected from the modelled fault geometry. The modern river channel should record the slip due to the single 1978 earthquake ( $\sim 5$  m vertical motion as seen from DEM differencing and our model), whereas T1 and T2 should record a cumulative fault slip from multiple earthquakes. We used the fault model from Section 5.1 to predict the uplift of the river channel and terraces. If the river channel only records the motion of the 1978 earthquakes, the uplift along profile S1–S1' can be determined from the Okada model (Okada, 1985) with a fault slip of 7 m. As shown in Fig. 9c, the modelled uplift is consistent with that measured ( $\sim 5.0$  m).

To estimate the fault slip responsible for the uplift of river terraces T1 and T2, we fixed the fault geometry, i.e. a fault plane dipping  $50^\circ$  beneath depths of 0.1 km to 6 km at its base, and varied the slip from 11–23 m in steps of 1 m (as shown in Fig. 9). To produce the uplift of T1 ( $\sim 9.5$  m), a fault slip of 13–14 m is needed. The uplift of T2 ( $\sim 14$  m) requires a fault slip of 21–22 m. Note that profile S3–S3' at the eastern end was drawn on the T1 surface, which causes underestimation of the uplift compared to that from the model. The inferred slip (13–14 m and 21–22 m) appears to be multiples of the slip in the 1978 earthquake (7 m), indicating that T1 and T2 possibly record two and three earthquakes, with a similar magnitude to the 1978 event. It is possible that the inferred slip was caused by more than three events with smaller magnitudes. If that was the case, we would expect to see more river terraces with smaller height changes. However, as we only observed two levels of river terrace, it is plausible that T1 and T2 simply record two and three repeated earthquakes respectively.

The good agreement between the modelled surface uplift and the measured folding suggests that the Tabas fold may exhibit characteristic slip behaviour. Such behaviour was also observed on the Hoshab fault in the eastern Makran from an investigation of the 2013  $M_w$  7.7 Balochistan earthquake (Zhou et al., 2015a), and the Fuyun fault in China (Klinger et al., 2011). As we do not have any direct measurements of the slip rate on the Tabas fault, we assume that the  $\sim 1.5$  mm/yr right-lateral strike-slip rate of the Nayband fault (Foroutan et al., 2014; Walker et al., 2009, 2013) is accommodated by repeated thrusting on the Tabas fold system ( $\sim 1$  mm/yr in the shortening direction). Given an average of  $\sim 3.5$  m shortening, as observed in the 1978 earthquake, it would require a magnitude  $M_w$  7.3 earthquake every  $\sim 3,500$  years. Future palaeoseismic studies are needed to confirm this. Nevertheless, we do not know the spatial extent of slip in the Tabas earthquake and hence the state of stress on neighbouring thrust faults. The 1978 Tabas earthquake could have brought neighbouring fault segments closer to failure. Better structure mapping and qualification of slip rates are required to better characterise the seismic hazard in this area.

## 6. Conclusions

Historical images have opened up new opportunities for studies of past earthquakes. In this study, we measured the horizontal motion associated with the 1978  $M_w$  7.3 Tabas earthquake using KH-9, SPOT-2 and SPOT-6 images, and the vertical motion using aerial photographs and SPOT-6 stereo imagery. The results are consistent and provide insights into the coseismic and long-lasting postseismic deformation. We found time-dependent shallow postseismic afterslip, decaying as  $\alpha t^n$  with a best-fitting power law exponent of 0.02. Although we do not have any constraints on the afterslip in the early postseismic period, it is very likely that most of the afterslip occurred prior to 1991. From comparison of terrace heights with the earthquake uplift, we also found that

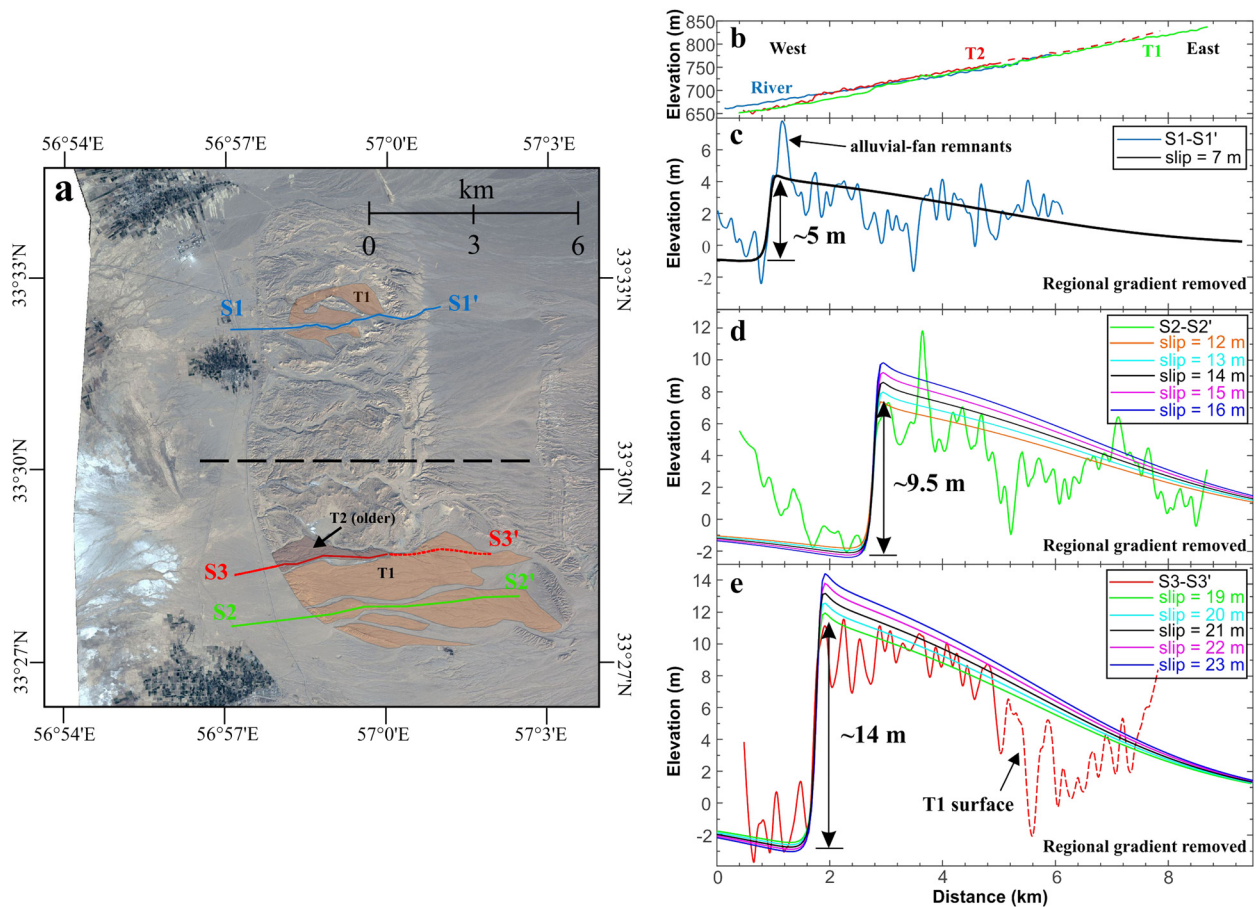


**Fig. 9.** Long-term surface folding of the Tabas fold. (a) SPOT-6 orthoimage showing the Tabas fold. We identified two river terraces (T1 and T2) from the image and the DEM derived from it. Topographic profiles S1–S1' (along a modern river channel), S2–S2' (along the T1 surface), and S3–S3' (along the T2 surface) were projected onto the fault-perpendicular direction (black dashed line). (b) Original topographic profiles from the SPOT-6 DEM. Blue, green and red lines indicate S1–S1', S2–S2' and S3–S3' respectively. (c) Topographic profile S1–S1' after removing a regional gradient. The black line is the predicted topography using the Okada model (Okada, 1985) and our estimated fault parameters (7 m slip on a 50° dipping fault, from a depth of 0.1 km to 6 km at its base). (d) Topographic profile S2–S2' after removing a regional gradient. The predicted topography assume a model with a uniform slip (12–16 m in steps of 1 m) on a 50° dipping fault, from a depth of 0.1 km to 6 km at its base. (e) Topographic profile S3–S3' after removing a regional gradient. The predicted topography assume a model of a uniform slip (19–23 m in steps of 1 m) on a 50° dipping fault, from a depth of 0.1 km to 6 km at its base.

the Tabas fold system may exhibit a characteristic slip behaviour. This behaviour requires a magnitude  $M_w$  7.3 earthquake every ~3500 years to accommodate the previously estimated shortening rate of ~1.0 mm/yr. This study potentially provides a means to investigate palaeoseismology of the Tabas folds, despite a lack of obvious surface scarps. The method may be useful more generally in regions of fault-related folding.

### Acknowledgements

This work was supported by the University of Oxford through a PAG scholarship to Yu Zhou, the National Natural Science Foundation of China (No. 41204027) to Xiaogang Song, and the Natural Environment Research Council through the NERC/ESRC Earthquakes without Frontiers (EwF) consortium, the Looking into the Continents from Space (LiCS) large grant (NE/K011006/1) and the Centre for the Observation and Modelling of Earthquakes, Volcanoes and Tectonics (COMET).

### Appendix A. Supplementary material

Supplementary material related to this article can be found online at <http://dx.doi.org/10.1016/j.epsl.2016.07.038>.

### References

- Astrium, 2013. SPOT 6 & SPOT 7 imagery user guide. Astrium GEO-Information Services, Toulouse, France. 120 pp.
- Ayoub, F., Leprince, S., Keene, L., 2009. Users guide to COSI-CORR co-registration of optically sensed images and correlation. California Institute of Technology, Pasadena, CA, USA, p. 38.
- Barišini, I., Hinojosa-Corona, A., Parsons, B., 2015. Co-seismic vertical displacements from a single post-seismic lidar DEM: example from the 2010 El Mayor–Cucapah earthquake. *Geophys. J. Int.* 202 (1), 328–346. <http://dx.doi.org/10.1093/gji/ggv139>.
- Berberian, M., 1979. Earthquake faulting and bedding thrust associated with the Tabas-e-Golshan (Iran) earthquake of September 16. *Bull. Seismol. Soc. Am.* 69 (6), 1861–1887.
- Berberian, M., 1981. Active faulting and tectonics of Iran. In: *Zagros Hindu Kush Himalaya Geodynamic Evolution*, pp. 33–69.
- Berberian, M., 1982. Aftershock tectonics of the 1978 Tabas-e-Golshan (Iran) earthquake sequence: a documented active 'thin- and thick-skinned tectonic' case. *Geophys. J. Int.* 68 (2), 499–530.
- Berberian, M., Asudeh, I., Bilham, R., Scholz, C., Soufleris, C., 1979. Mechanism of the main shock and the aftershock study of the Tabas-e-Golshan (Iran) earthquake of September 16, 1978: a preliminary report. *Bull. Seismol. Soc. Am.* 69 (6), 1851–1859.
- Brown, D.C., 1971. Close-range camera calibration. *Photogramm. Eng. Remote Sens.* 37, 855–866.
- Burbank, D.W., Anderson, R.S., 2011. *Tectonic Geomorphology*. John Wiley & Sons.
- Burnett, M.G., 2012. Hexagon (KH-9) – Mapping Camera Program and Evolution. National Reconnaissance Office (NRO), Center for the Study of National Reconnaissance (CSNR), Chantilly, VA, USA, p. 395.

- Çakir, Z., Ergintav, S., Özener, H., Dogan, U., Akoglu, A.M., Meghraoui, M., Reilinger, R., 2012. Onset of aseismic creep on major strike-slip faults. *Geology* 40 (12), 1115–1118.
- Copley, A., 2014. Postseismic afterslip 30 years after the 1978 Tabas-e-Golshan (Iran) earthquake: observations and implications for the geological evolution of thrust belts. *Geophys. J. Int.* <http://dx.doi.org/10.1093/gji/ggu023>.
- Dolan, J.F., Christofferson, S.A., Shaw, J.H., 2003. Recognition of paleoearthquakes on the Puente Hills blind thrust fault, California. *Science* 300 (5616), 115–118.
- Elliott, J., Jolivet, R., González, P., Avouac, J.-P., Hollingsworth, J., Searle, M., Stevens, V., 2016. Himalayan megathrust geometry and relation to topography revealed by the Gorkha earthquake. *Nat. Geosci.*
- England, P., Jackson, J., 2011. Uncharted seismic risk. *Nat. Geosci.* 4 (6), 348–349.
- Fattahi, M., Walker, R., Talebian, M., Sloan, R., Rasheedi, A., 2014. Late Quaternary active faulting and landscape evolution in relation to the Gowk Fault in the South Golbaf Basin, SE Iran. *Geomorphology* 204, 334–343. <http://dx.doi.org/10.1016/j.geomorph.2013.08.017>.
- Feng, G., Li, Z., Shan, X., Zhang, L., Zhang, G., Zhu, J., 2015. Geodetic model of the 2015 April 25  $M_w$  7.8 Gorkha Nepal Earthquake and  $M_w$  7.3 aftershock estimated from InSAR and GPS data. *Geophys. J. Int.* 203 (2), 896–900.
- Fialko, Y., Sandwell, D., Simons, M., Rosen, P., 2005. Three-dimensional deformation caused by the Bam, Iran, earthquake and the origin of shallow slip deficit. *Nature* 435 (7040), 295–299.
- Foroutan, M., Meyer, B., Sébrier, M., Nazari, H., Murray, A., Le Dortz, K., Shokri, M., Arnold, M., Aumaître, G., Bourlès, D., et al., 2014. Late Pleistocene–Holocene right slip rate and paleoseismology of the Nayband fault, western margin of the Lut block, Iran. *J. Geophys. Res., Solid Earth* 119 (4), 3517–3560. <http://dx.doi.org/10.1002/2013JB010746>.
- Freed, A.M., Bürgmann, R., Calais, E., Freymueller, J., 2006. Stress-dependent power-law flow in the upper mantle following the 2002 Denali, Alaska, earthquake. *Earth Planet. Sci. Lett.* 252 (3), 481–489.
- Funning, G.J., Parsons, B., Wright, T.J., Jackson, J.A., Fielding, E.J., 2005. Surface displacements and source parameters of the 2003 Bam (Iran) earthquake from Envisat advanced synthetic aperture radar imagery. *J. Geophys. Res., Solid Earth* 110 (B9).
- Grandin, R., Vallée, M., Satriano, C., Lacassin, R., Klinger, Y., Simoes, M., Bollinger, L., 2015. Rupture process of the  $M_w = 7.9$  2015 Gorkha earthquake (Nepal): insights into Himalayan megathrust segmentation. *Geophys. Res. Lett.* 42 (20), 8373–8382.
- Gratier, J.P., Renard, F., Vial, B., 2014. Postseismic pressure solution creep: evidence and time-dependent change from dynamic indenting experiments. *J. Geophys. Res., Solid Earth* 119 (4), 2764–2779. <http://dx.doi.org/10.1002/2013JB010768>.
- Hessami, K., 2002. Tectonic History and Present-Day Deformation in the Zagros Fold-Thrust Belt. *Acta Universitatis Upsaliensis*.
- Hollingsworth, J., Jackson, J., Walker, R., Nazari, H., 2008. Extrusion tectonics and subduction in the eastern South Caspian region since 10 Ma. *Geology* 36 (10), 763–766.
- Hollingsworth, J., Leprince, S., Ayoub, F., Avouac, J.-P., 2012. Deformation during the 1975–1984 Krafla rifting crisis, NE Iceland, measured from historical optical imagery. *J. Geophys. Res., Solid Earth* (1978–2012) 117 (B11). <http://dx.doi.org/10.1029/2012JB009140>.
- Hubbard, J., Shaw, J.H., 2009. Uplift of the Longmen Shan and Tibetan plateau, and the 2008 Wenchuan ( $M = 7.9$ ) earthquake. *Nature* 458 (7235), 194–197.
- Jackson, J., 2001. Living with earthquakes: know your faults. *J. Earthq. Eng.* 5 (spec01), 5–123.
- Jackson, J., Haines, J., Holt, W., 1995. The accommodation of Arabia–Eurasia plate convergence in Iran. *J. Geophys. Res., Solid Earth* (1978–2012) 100 (B8), 15,205–15,219.
- Kirby, S.H., 1983. Rheology of the lithosphere. *Rev. Geophys.* 21 (6), 1458–1487.
- Klinger, Y., Etchebes, M., Tapponnier, P., Narteau, C., 2011. Characteristic slip for five great earthquakes along the Fuyun fault in China. *Nat. Geosci.* 4 (6), 389–392.
- Leprince, S., Barbot, S., Ayoub, F., Avouac, J.-P., 2007. Automatic and precise orthorectification, coregistration, and subpixel correlation of satellite images, application to ground deformation measurements. *IEEE Trans. Geosci. Remote Sens.* 45 (6), 1529–1558.
- Meyer, B., Le Dortz, K., 2007. Strike-slip kinematics in central and eastern Iran: estimating fault slip-rates averaged over the Holocene. *Tectonics* 26 (5).
- Mollberg, B., Schardt, B., 1988. Mission report on the Orbiter Camera Payload System (OCPS) Large Format Camera (LFC) and Attitude Reference System (ARS).
- Molnar, P., Lyon-Caen, H., 1989. Fault plane solutions of earthquakes and active tectonics of the Tibetan Plateau and its margins. *Geophys. J. Int.* 99 (1), 123–153.
- Molnar, P., Fitch, T.J., Wu, F.T., 1973. Fault plane solutions of shallow earthquakes and contemporary tectonics in Asia. *Earth Planet. Sci. Lett.* 19 (2), 101–112.
- Mousavi, Z., Walpersdorf, A., Walker, R., Tavakoli, F., Pathier, E., Nankali, H., Nilfouroushan, F., Djamour, Y., 2013. Global Positioning System constraints on the active tectonics of NE Iran and the South Caspian region. *Earth Planet. Sci. Lett.* 377, 287–298.
- Okada, Y., 1985. Surface deformation due to shear and tensile faults in a half-space. *Bull. Seismol. Soc. Am.* 75 (4), 1135–1154.
- Oskin, M.E., Arrowsmith, J.R., Corona, A.H., Elliott, A.J., Fletcher, J.M., Fielding, E.J., Gold, P.O., Garcia, J.J.G., Hudnut, K.W., Liu-Zeng, J., Teran, O.J., 2012. Near-field deformation from the El Mayor–Cucapah earthquake revealed by differential LiDAR. *Science* 335 (6069), 702–705.
- Pollitz, F.F., 2005. Transient rheology of the upper mantle beneath central Alaska inferred from the crustal velocity field following the 2002 Denali earthquake. *J. Geophys. Res., Solid Earth* 110 (B8).
- Regard, V., Bellier, O., Braucher, R., Gasse, F., Bourlès, D., Mercier, J., Thomas, J.-C., Abbassi, M., Shabanian, E., Soleymani, S., 2006.  $^{10}\text{Be}$  dating of alluvial deposits from Southeastern Iran (the Hormoz Strait area). *Palaeogeogr. Palaeoclimatol. Palaeoecol.* 242 (1), 36–53.
- Scholz, C.H., 1982. Scaling laws for large earthquakes: consequences for physical models. *Bull. Seismol. Soc. Am.* 72 (1), 1–14.
- Segall, P., Bürgmann, R., Matthews, M., 2000. Time-dependent triggered afterslip following the 1989 Loma Prieta earthquake. *J. Geophys. Res., Solid Earth* (1978–2012) 105 (B3), 5615–5634.
- Suito, H., Freymueller, J.T., 2009. A viscoelastic and afterslip postseismic deformation model for the 1964 Alaska earthquake. *J. Geophys. Res., Solid Earth* (1978–2012) 114 (B11).
- Surazakov, A., Aizen, V., 2010. Positional accuracy evaluation of declassified Hexagon KH-9 mapping camera imagery. *Photogramm. Eng. Remote Sens.* 76 (5), 603–608.
- Tapponnier, P., Meyer, B., Avouac, J.P., Peltzer, G., Gaudemer, Y., Shunmin, G., Hongfa, X., Kelun, Y., Zhitai, C., Shuahu, C., et al., 1990. Active thrusting and folding in the Qilian Shan, and decoupling between upper crust and mantle in northeastern Tibet. *Earth Planet. Sci. Lett.* 97 (3), 382–403.
- Tatar, M., Hatzfeld, D., Martinod, J., Walpersdorf, A., Ghafori-Ashtiani, M., Chéry, J., 2002. The present-day deformation of the central Zagros from GPS measurements. *Geophys. Res. Lett.* 29 (19), 33–1.
- Vallage, A., Klinger, Y., Grandin, R., Bhat, H., Pierrot-Deseilligny, M., 2015. Inelastic surface deformation during the 2013  $M_w$  7.7 Balochistan, Pakistan, earthquake. *Geology* 43 (12), 1079–1082.
- Vernant, P., Nilfouroushan, F., Hatzfeld, D., Abbassi, M., Vigny, C., Masson, F., Nankali, H., Martinod, J., Ashtiani, A., Bayer, R., et al., 2004a. Present-day crustal deformation and plate kinematics in the Middle East constrained by GPS measurements in Iran and northern Oman. *Geophys. J. Int.* 157 (1), 381–398.
- Vernant, P., Nilfouroushan, F., Chéry, J., Bayer, R., Djamour, Y., Masson, F., Nankali, H., Ritz, J.-F., Sedighi, M., Tavakoli, F., 2004b. Deciphering oblique shortening of central Alborz in Iran using geodetic data. *Earth Planet. Sci. Lett.* 223 (1), 177–185.
- Walker, R., Jackson, J., 2004. Active tectonics and late Cenozoic strain distribution in central and eastern Iran. *Tectonics* 23 (5).
- Walker, R., Jackson, J., Baker, C., 2003. Surface expression of thrust faulting in eastern Iran: source parameters and surface deformation of the 1978 Tabas and 1968 Ferdows earthquakes sequences. *Geophys. J. Int.* 152 (3), 749–765.
- Walker, R., Gans, P., Allen, M., Jackson, J., Khatib, M., Marsh, N., Zarrinkoub, M., 2009. Late Cenozoic volcanism and rates of active faulting in eastern Iran. *Geophys. J. Int.* 177 (2), 783–805.
- Walker, R., Khatib, M., Bahroudi, A., Rodés, A., Schnabel, C., Fattahi, M., Talebian, M., Bergman, E., 2013. Co-seismic, geomorphic, and geologic fold growth associated with the 1978 Tabas-e-Golshan earthquake fault in eastern Iran. *Geomorphology* 237, 98–118.
- Walpersdorf, A., Hatzfeld, D., Nankali, H., Tavakoli, F., Nilfouroushan, F., Tatar, M., Vernant, P., Chéry, J., Masson, F., 2006. Difference in the GPS deformation pattern of North and Central Zagros (Iran). *Geophys. J. Int.* 167 (3), 1077–1088.
- Walpersdorf, A., Manighetti, I., Mousavi, Z., Tavakoli, F., Vergnolle, M., Jadidi, A., Hatzfeld, D., Aghamohammadi, A., Bigot, A., Djamour, Y., et al., 2014. Present-day kinematics and fault slip rates in eastern Iran, derived from 11 years of GPS data. *J. Geophys. Res., Solid Earth* 119 (2), 1359–1383. <http://dx.doi.org/10.1002/2013JB010620>.
- Wang, K., Fialko, Y., 2015. Slip model of the 2015  $M_w$  7.8 Gorkha (Nepal) earthquake from inversions of ALOS-2 and GPS data. *Geophys. Res. Lett.* 42 (18), 7452–7458.
- Yu, S.-B., Hsu, Y.-J., Kuo, L.-C., Chen, H.-Y., Liu, C.-C., 2003. GPS measurement of post-seismic deformation following the 1999 Chi-Chi, Taiwan, earthquake. *J. Geophys. Res., Solid Earth* 108 (B11).
- Zhang, P.-Z., 2013. Beware of slowly slipping faults. *Nat. Geosci.* 6 (5), 323–324.
- Zhou, Y., Elliott, J.R., Parsons, B., Walker, R.T., 2015a. The 2013 Balochistan earthquake: an extraordinary or completely ordinary event? *Geophys. Res. Lett.* 42 (15), 6236–6243. <http://dx.doi.org/10.1002/2015GL065096>.
- Zhou, Y., Parsons, B., Elliott, J.R., Barisin, I., Walker, R.T., 2015b. Assessing the ability of Pleiades stereo imagery to determine height changes in earthquakes: a case study for the El Mayor–Cucapah epicentral area. *J. Geophys. Res., Solid Earth* 120 (12), 8793–8808. <http://dx.doi.org/10.1002/2015JB012358>.